A full-particle Martian upper thermosphere-exosphere model using the DSMC method

Kaori Terada, Naoki Terada, Hiroyuki Shinagawa, Hitoshi Fujiwara, Yasumasa Kasaba, Kanako Seki, François Leblanc, Jean-Yves Chaufray, Ronan Modolo

AGU PUBLICATIONS

JGR

Journal of Geophysical Research: Planets

RESEARCH ARTICLE
10.1002/2015JE004961

Key Points:
- A full-particle Martian upper thermosphere-exosphere model has been developed
- Heating efficiency of the upper thermosphere is essentially the same for 1 EUV and 6 EUV cases
- Applying different models of the CO_2 15 um cooling rate leads to difference in the exobase temperature by 150 K for 6 EUV case

Correspondence to:
K. Terada,
kaneda@pat.gp.tohoku.ac.jp

Citation:
Terada, K., N. Terada, H. Shinagawa, H. Fujiwara, Y. Kasaba, K. Seki, F. Leblanc, J.-Y. Chaufray, and R. Modolo (2016), A full-particle Martian upper thermosphere-exosphere model using the DSMC method, *J. Geophys. Res. Planets*, *121*, 1429–1444, doi:10.1002/2015JE004961.

Received 19 OCT 2015
Accepted 5 AUG 2016
Accepted article online 9 AUG 2016
Published online 23 AUG 2016

A full-particle Martian upper thermosphere-exosphere model using the DSMC method

Kaori Terada[1], Naoki Terada[1], Hiroyuki Shinagawa[2], Hitoshi Fujiwara[3], Yasumasa Kasaba[1], Kanako Seki[4], François Leblanc[5], Jean-Yves Chaufray[5], and Ronan Modolo[5]

[1]Department of Geophysics, Graduate School of Science, Tohoku University, Miyagi, Japan, [2]Space Environment Group, Applied Electromagnetic Research Center, National Institute of Information and Communications Technology, Tokyo, Japan, [3]Faculty of Science and Technology, Seikei University, Tokyo, Japan, [4]Department of Earth and Planetary Science, Graduate School of Science, University of Tokyo, Tokyo, Japan, [5]LATMOS/IPSL, CNRS, Universite Pierre et Marie Curie, Paris, France

Abstract A one-dimensional full-particle model of the Martian upper thermosphere-exosphere has been developed, where the Direct Simulation Monte Carlo (DSMC) method is applied to both thermal and nonthermal components. Our full-particle model can self-consistently solve the transition from collisional to collisionless domains in the upper thermosphere, so that the energy deposition from nonthermal energetic components to thermal components in the transition region is properly described. For the solar EUV condition during the Viking 1 measurement (1 EUV case), computed density profiles are in good agreement with those observed by Viking 1 and with the conventional model. For a solar EUV flux 6 times the Viking 1 condition (6 EUV case), the computed heating efficiency is essentially the same as the 1 EUV case but slightly increases by about 10% below the exobase, and temperature deviates from the conventional model in and above the transition region. This result suggests that the conventional heating efficiency of 0.18 is a good approximation for low (1 EUV case) to moderately strong (6 EUV case) solar EUV conditions but would be inappropriate for an extremely strong solar EUV (up to ~100 times stronger flux) environment. We also find that applying different models of the CO_2-O collisional energy transfer rate results in a difference in the calculated exobase temperature by 150 K for the 6 EUV case.

1. Introduction

It has been proposed that atmospheric escape has played a significant role in the evolution of the Martian atmosphere [e.g., *Lammer et al.*, 2003]. Two types of atmospheric escape processes have been proposed: thermal escape and nonthermal escape [see *Shizgal and Arkos*, 1996, and references therein]. Thermal escape is loss of a planetary atmosphere driven by the local temperature, and is particularly effective for light molecular species, like hydrogen. This escape process is called "Jeans escape" or "evaporative escape." At the present-day Martian exobase, the most energetic part of the Maxwell-Boltzmann velocity distribution of hydrogen exceeds the escape velocity and thus Jeans escape operates [e.g., *Chaufray et al.*, 2015]. On the other hand, heavy molecular species, like oxygen, escape through nonthermal escape processes. Nonthermal escape is the loss of energetic particles produced by exothermic chemical reactions (e.g., the dissociative recombination of O_2^+) [*McElroy*, 1972; *Ip*, 1988; *Nagy and Cravens*, 1988; *Lammer and Bauer*, 1991; *Fox*, 1993; *Zhang et al.*, 1993; *Luhmann*, 1997; *Kim et al.*, 1998; *Hodges*, 2000; *Lammer et al.*, 2000; *Cipriani et al.*, 2007; *Chaufray et al.*, 2007; *Kaneda et al.*, 2007, 2009; *Valeille et al.*, 2009a, 2009b, 2010a, 2010b; *Yagi et al.*, 2012; *Fox and Haćić*, 2010, 2014; *Gröller et al.*, 2014; *Lee et al.*, 2015], by collisions with incident energetic particles, called "sputtering" [*Luhmann and Kozyra*, 1991; *Luhmann et al.*, 1992; *Leblanc and Johnson*, 2001, 2002; *Cipriani et al.*, 2007; *Chaufray et al.*, 2007], by accelerations in the electromagnetic fields following ionizations of neutral atmosphere, called "ion pickup"' or "cold ion outflow" [*Lundin et al.*, 1989, 2008; *Perez-de-Tejada*, 1987, 1992; *Modolo et al.*, 2005; *Terada et al.*, 2009], and so on.

Simulation studies of the Martian thermosphere and exosphere under solar EUV fluxes of one, three, and six times the present-day value, which correspond to the present time, ~2.7 Gyr ago, and ~3.6 Gyr ago, respectively, have been conducted in order to estimate the evolution of the atmospheric outflow over the Martian history [*Zhang et al.*, 1993; *Luhmann*, 1997; *Lammer et al.*, 2003; *Valeille et al.*, 2009b, 2010b]. Conventionally, the escape of thermal and nonthermal components of the Martian thermosphere and exosphere has been studied using different models. Thermal components are solved in a model that employs a fluid approximation, and nonthermal components are solved with a two-stream model or a Monte Carlo

Table 1. Chemical Reaction Rates Used in the Ionosphere Model

Reaction	Rate Coefficient ($cm^3\ s^{-1}$)	Reference
$O^+ + CO_2 \rightarrow O_2^+ + CO$	1.10×10^{-9}	*Fox and Sung* [2001]
$O^+ + N_2 \rightarrow NO^+ + N$	$1.20 \times 10^{-12}\ (300/T_i)^{0.45}$	*Fox and Sung* [2001]
$O^+ + H \rightarrow H^+ + O$	6.40×10^{-10}	*Fox and Sung* [2001]
$CO_2^+ + O \rightarrow O_2^+ + CO$	1.64×10^{-10}	*Schunk and Nagy* [1980]
$CO_2^+ + O \rightarrow O^+ + CO_2$	9.60×10^{-11}	*Schunk and Nagy* [1980]
$H^+ + O \rightarrow O^+ + H$	$2.2 \times 10^{-11} T_i^{0.5}$	*Schunk and Nagy* [1980]
$H^+ + CO_2 \rightarrow CHO^+ + O$	3.0×10^{-9}	*Schunk and Nagy* [1980]
$CO_2^+ + e \rightarrow O + CO$	$3.5 \times 10^{-7}\ (300/T_e)^{0.5}$	*Fox and Sung* [2001]
$O_2^+ + e \rightarrow O + O$	$2.4 \times 10^{-7}\ (300/T_e)^{0.7}$	*Peverall et al.* [2000]

particle model. Simulation studies of nonthermal components have demonstrated that the energetic O atoms produced by the dissociative recombination of O_2^+ at an altitude far below the exobase are not well thermalized, and some of them escape to space [e.g., *Fox and Hać*, 2010]. The thermalization of nonthermal components is an important heat source for the thermal components. Hot O created by the dissociative recombination of O_2^+ is thought to be the primary heating source in the upper thermosphere at the current epoch [*Fox and Dalgarno*, 1979]. In the regions where nonthermal components are not thermalized immediately, "nonlocal" processes in the energy deposition from the nonthermal to thermal components can be important, i.e., hot O atoms that were originally produced in lower altitude can deposit their energy into thermal components in and above the transition region. In such a situation, a detailed study of the heating process that takes into account the spatial variation of the velocity distributions of both thermal and nonthermal components is required. It is often inappropriate to use macroscopic parameters such as a heating efficiency because they do not consider the nonlocal processes around the transition region. Therefore, it is desirable that both thermal and nonthermal components be simultaneously solved in a particle model.

The Direct Simulation Monte Carlo (DSMC) method is a particle simulation technique for solving the Boltzmann equation [e.g., *Bird*, 1994]. It is an effective approach for simulating the transition between collisional and collisionless domains, where the momentum exchange in a collision between atmospheric particles is still important and a nonthermal component is substantially present. Recently, the DSMC method was used to solve nonthermal components in the Martian thermosphere-exosphere, but thermal components were still described using a fluid approximation [*Valeille et al*., 2009a, 2009b, 2010a, 2010b; *Lee et al*., 2014a, 2014b, 2015].

In this paper, we present a full-particle model of the Martian upper thermosphere and exosphere, where the DSMC method is applied to both thermal and nonthermal components. It is a major feature of this DSMC model that the primary heating source in the upper thermosphere of Mars, i.e., the dissociative recombination of O_2^+, is self-consistently solved, while other minor heating sources such as quenching [*Fox and Dalgarno*, 1979] are included using a macroscopic heating efficiency. Computed altitude profiles of densities and temperatures of thermal components are compared to those measured by Viking 1 and to those calculated by a model using the conventional heating efficiency of 0.18 [*Zhang et al*., 1993] for two cases: Solar EUV fluxes equivalent to the Viking 1 condition (hereinafter referred to as the 1 EUV case) and 6 times the Viking 1 condition (hereinafter referred to as the 6 EUV case). Six times the solar EUV flux corresponds to the luminosity of the Sun about 3.6 Gyr ago [*Zahnle and Walker*, 1982; *Ribas et al*., 2005].

2. Model Description

A one-dimensional full-particle model using the DSMC approach coupled with a photochemical equilibrium ionosphere model is used for modeling the Martian dayside upper thermosphere and exosphere. The DSMC model determines the number of production and the nascent positions and velocities of energetic O atoms produced by the O_2^+ dissociative recombination. The ionosphere model obtains the number densities of major ions and electrons. A simultaneous coupling between the DSMC model and the ionosphere model is achieved by passing the densities and temperatures of neutral molecules calculated from the DSMC model as inputs to the ionosphere model to calculate the reaction rates in Table 1 (ion and electron temperatures are obtained using neutral temperatures as explained below) and by passing the densities and temperatures

of O_2^+ ions and electrons calculated from the ionosphere model as inputs to the DSMC model to calculate the O_2^+ dissociative recombination rate (see equation (10)). Brief descriptions of the models are given below.

3. DSMC Model

The lower boundary of the model is located at 130 km, where the Knudsen number is about 0.01 for the Viking 1 condition, and the upper boundary is situated at 1000 km, where the Knudsen number is much larger than 10. Here the Knudsen number is defined as the ratio of the mean free path of a molecular species to the scale height of the atmosphere.

The DSMC model simulates the positions and velocities of model particles under the influence of collisions among themselves and the planets gravity field. The model particles represent four species: CO_2 and O, the main species in the Martian upper thermosphere, and N_2 and H, required to calculate the densities of the major ion species in the ionosphere model (see chemical reactions in Table 1). Although CO is also an important species for the thermalization of hot O [*Lee et al.*, 2015] and Mars Atmosphere and Volatile EvolutioN Mission (MAVEN) recently detected O_2 and other minor species in the upper atmosphere of Mars [*Mahaffy et al.*, 2015], CO, O_2, and other minor species are not included in the current version of the model for simplicity. The strategy of the DSMC method is to decouple the convection and collision calculations. This approach requires that a time step be shorter than the mean time between collisions. In this model, the time step is set to 0.01 s, about a quarter of the minimum mean time between collisions above 130 km altitude. The macroscopic quantities, such as number density (n), flow velocity ($\boldsymbol{v}$), and temperature (T), are obtained through statistical averaging over 100,000 s to reduce statistical errors.

$$n = \frac{wN}{V} \tag{1}$$

$$v = \frac{1}{N}\sum_i c_i \tag{2}$$

$$T = \frac{m}{3k_B N}\sum_i (c_i - v)^2 \tag{3}$$

where w is the particle weight; N is the number of model particles in a cell; V is the volume of a cell; $\boldsymbol{c}_i$ is the velocity of a model particle i; m is the mass; k_B is the Boltzmann constant. The particle weights are $w[\mathrm{H}] = 1.7\times10^{11}$, $w[CO_2] = 1.0\times10^{15}$, $w[N_2] = 1.5\times10^{14}$, w[thermal O] $= 3.0\times10^{14}$, and w[hot O] $= 2.04\times10^{10}$ (real particles/a model particle). Here a "hot O" is defined as a particle produced by the O_2^+ dissociative recombination and its kinetic energy is larger than $2.5k_BT_{\mathrm{thermalO}}$. When the energy of a hot O particle falls below the threshold energy after collisions with the thermospheric species, it has a negligible contribution to the heating of the thermal component. A hot O particle is converted to a thermal O particle with a probability determined by the ratio of the particle weights (i.e., $100\times w$[hot O]/w[thermal O] percent) [cf. *Nanbu and Yonemura*, 1998], if its energy becomes less than the threshold energy. A thermal O particle sometimes gains enough energy to escape after colliding with a hot O particle. The secondary hot O contributes ~10–20% of photochemical escape rate [*Lee et al.*, 2015]. However, the current simple DSMC model is not able to estimate the escape rate from the secondary hot O accurately, because the weight of the thermal O that gained enough energy to become a hot O is too large.

In order to describe the molecular collisions in the model, we employ the variable sphere model [*Matsumoto*, 2002]. In this model, the total cross section (σ_t) and the deflection angle (χ_0) are defined using diffusion and viscosity cross sections.

$$\sigma_t = \frac{\sigma_d}{2\sigma_d - \sigma_v}\sigma_d, \tag{4}$$

$$\cos\chi_o = \frac{\sigma_v - \sigma_d}{\sigma_d}, \tag{5}$$

where σ_d and σ_v are the diffusion and viscosity cross sections, respectively. The collision model is simple and efficient, and both diffusion and viscosity cross sections are consistent with the intermolecular potential and calculated as described below.

Table 2. Parameters of the Lennard-Jones (6–12) Potential Used in the Molecular Dynamics Calculations[a]

Molecule	σ (Å)	ε/k_B (K)	Reference
H	2.708	37.0	*Svehla* [1962]
O	2.80	117.0	*Capitelli et al.* [2000]
N_2	3.681	91.42	*Capitelli et al.* [2000]
CO_2	3.769	245.3	*Boushehri et al.* [1987]

[a] σ is the value of the intermolecular distance for which the potential is zero, and ε is the depth of the potential well.

The diffusion and viscosity cross sections of collisions between molecules were computed by molecular dynamics calculations before running the DSMC simulation. The Lennard-Jones (6–12) potential is used to represent the interaction between two molecules. The Lennard-Jones (6–12) potential parameters used in this work are summarized in Table 2. Intermolecular potential parameters for heteromolecular systems are derived using the combination laws described as [*Chapman and Cowling*, 1970; *Hirschfelder et al*., 1964]

$$\sigma_{ij} = \frac{\sigma_{ii} + \sigma_{jj}}{2}, \tag{6}$$

$$\varepsilon_{ij} = \sqrt{\varepsilon_{ii} \cdot \varepsilon_{jj}} \tag{7}$$

where σ_{ij} and ε_{ij} are the values of the intermolecular distance for which the potential is zero and the depth of the potential well between molecules of species i and j, respectively. Polyatomic molecules are treated as rigid units, assuming internal energy conservation in the intermolecular interaction.

The diffusion and viscosity cross sections are defined as functions of collision energy E. They are described as

$$\sigma_d(E) \equiv 2\pi \int_0^\infty (1 - \cos\chi(E,b)) b db \approx 2\pi \sum_{b=0}^{1.5\times10^4} (1 - \cos\chi(E,b)) b \Delta b, \tag{8}$$

$$\sigma_v(E) \equiv 2\pi \int_0^\infty \left(1 - \cos^2\chi(E,b)\right) b db \approx 2\pi \sum_{b=0}^{1.5\times10^4} \left(1 - \cos^2\chi(E,b)\right) b \Delta b, \tag{9}$$

where χ is the deflection angle and b is the impact parameter. We computed the deflection angles for 120 collision energies up to 10 eV and 15,000 impact parameter values up to 1.5 nm. The interval of b is 1.0×10^{-13} m. The yield diffusion and viscosity cross sections calculated using equations (8) and (9) are discretized with 120 collision energies and interpolated linearly when used in the DSMC simulation.

The heating and cooling mechanisms considered in the DSMC model are the dissociative recombination of O_2^+, other minor heating sources are quenching and chemical reactions [*Fox and Dalgarno*, 1979], CO_2 15 μm cooling, and molecular conduction. The primary heat balance occurs between the EUV heating and the molecular thermal conduction, with a little influence from the CO_2 15 μm cooling [*Bougher and Dickinson*, 1988; *Bougher and Roble*, 1991; *Gonzalez-Galindo et al*., 2009]. The heating by chemical reactions accounts for about 75% of the total EUV heating in which the dissociative recombination of O_2^+ accounts for 70% [*Fox and Dalgarno*, 1979].

At every time step, the model particles representing the hot O population are added to the system. The number, position, and velocity of the newly produced particles are determined using the densities and temperatures of O_2^+ ions and electrons calculated by the photochemical ionosphere model. Below the exobase level, more than 80% of O_2^+ ions are found to be in the vibrational ground state [*Fox and Hać*, 2010]. Because most of the hot O atoms that heat the ambient atmosphere or escape to space are produced below the exobase, we assume that all the O_2^+ ions are in $v = 0$. Five exothermic channels are available for O_2^+ ($v = 0$) in zero relative energy collisions with electrons:

$$\begin{aligned} O_2^+ + e &\rightarrow O(^3P) + O(^3P) + [6.65\ \text{eV}] \quad (0.22) \\ &\rightarrow O(^3P) + O(^1D) + [4.98\ \text{eV}] \quad (0.42) \\ &\rightarrow O(^1D) + O(^1D) + [3.02\ \text{eV}] \quad (0.31) \\ &\rightarrow O(^3P) + O(^1S) + [2.80\ \text{eV}] \quad (0.00) \\ &\rightarrow O(^1D) + O(^1S) + [0.80\ \text{eV}] \quad (0.05), \end{aligned} \tag{10}$$

where the square and round brackets denote excess energies and branching ratios used in this study, respectively. The values of the excess energies and the branching ratios are taken from *Peverall et al*. [2000]

and *Kella et al*. [1997], respectively. The excess energy is transferred into the kinetic energy of two produced hot O atoms. The nascent velocities of produced hot O atoms are determined by the conservation of momentum, assuming that these atoms are produced isotropically. The velocities of reactants, O_2^+ ions and electrons, are randomly selected from the Maxwell-Boltzmann distributions.

Our particle simulation model self-consistently includes the major heating and cooling sources, i.e., the dissociative recombination of O_2^+ and the energy transfer through collisions. Meanwhile, our rigid molecular model cannot describe variations in the internal energy of a molecule. Therefore, minor heating and cooling sources like quenching and the CO_2 15 μm cooling are added using macroscopic quantities such as number density, flow velocity, and temperature obtained from equations (1)–(3). For example, in our model the CO_2 15 μm cooling rate is calculated using the formula in equation (14) of *Gordiets et al*. [1982], which is a function of the number densities of CO_2, N_2, O, and other major species and the temperature of CO_2. The minor heating or cooling rate is added or removed from the thermal energies of the corresponding molecular species in each cell. The energy addition or removal is performed such that momentum is conserved on average:

$$c_i' = v + a(c_i - v)$$
$$\mathrm{a} = \sqrt{1 + \frac{2Q\mathrm{d}t}{\sum_{i=1}^{N} m(c_\mathrm{i} - v)^2}}, \tag{11}$$

where c_i' is the velocity of a model particle i after the energy addition or removal; $\boldsymbol{c}_i$ is the velocity of a model particle i before the energy addition or removal; $\boldsymbol{v}$ is the flow velocity calculated from equation (2); Q is the macroscopic heating rate (positive value) or macroscopic cooling rate (negative value); dt is the time step; m is the mass; N is the number of model particles in a cell; a is the coefficient for velocity variation. Here "macroscopic" heating or cooling rate means that it is a function of macroscopic quantities n, $\boldsymbol{v}$, and T, and does not consider the detail of the distribution in velocity space. The macroscopic heating rate is calculated using the heating efficiency of 0.08, which is derived from the relative importance of the heating processes in Figure 16 of *Fox and Dalgarno* [1979] and based on the hypothesis that the total heating efficiency including the dissociative recombination of O_2^+ is 0.18 for the present-day Martian upper thermosphere. This total heating efficiency of 0.18 is the same as the value used in *Zhang et al*. [1993]. The macroscopic cooling rate owing to the CO_2 15 μm cooling is calculated using the formula in *Gordiets et al*. [1982] with the collisional energy transfer rate of $k(CO_2\text{-}N_2) = 4.4/3 \times 10^{-15}\ T \exp(-41/T^{1/3})$ cm^3 s^{-1} and $k(CO_2\text{-}O) = 1.5 \times 10^{-11}\ T \exp(-800/T)$ cm^3 s^{-1}. We omit CO_2-O_2 collisional relaxation for simplicity, although recent MAVEN observations showed that O_2 is not minor [*Mahaffy et al*., 2015], suggesting that contribution from the CO_2-O_2 collisional relaxation can be comparable to that from CO_2-N_2 collisions.

At the lower boundary (130 km altitude) for the Viking 1 condition (1 EUV case), the number densities are fixed with $n[\mathrm{H}] = 1.088 \times 10^{11}$ m^{-3}, $n[CO_2] = 3.045 \times 10^{16}$ m^{-3}, $n[N_2] = 8.402 \times 10^{14}$ m^{-3}, and $n[\mathrm{O}] = 3.447 \times 10^{14}$ m^{-3}, and the temperature is fixed at 158 K. These values are based on the Viking measurements [*Nier and McElroy*, 1977; *Shinagawa and Cravens*, 1989]. For the 6 EUV case, the number density of O is fixed with 8.0×10^{14} m^{-3}, and the temperature is fixed at 280 K. These values are based on *Zhang et al*. [1993]. The other parameters are the same as those for the 1 EUV case. An appropriate number of model particles, with velocities selected from a Maxwell-Boltzmann distribution, flow in from the lower boundary at every time step. The number flux of model particles that flow in from the lower boundary is described as [*Bird*, 1994]

$$f_{in} = \frac{n}{2\sqrt{\pi}} \sqrt{\frac{2k_B T}{m}}. \tag{12}$$

The flow velocity is assumed to be zero at the lower boundary. Model particles that cross the upper or lower boundary stop being tracked. When a particle crosses the upper boundary with an energy lower than the escape energy at that altitude, it is reflected without a time lag since we are interested in the system in a (quasi-)steady state.

The initial condition of the system is a vacuum; i.e., the computational domain is empty at the beginning. The simulation ends at $t = 500{,}000$ s for the 1 EUV case and $t = 350{,}000$ s for the 6 EUV case, when the system

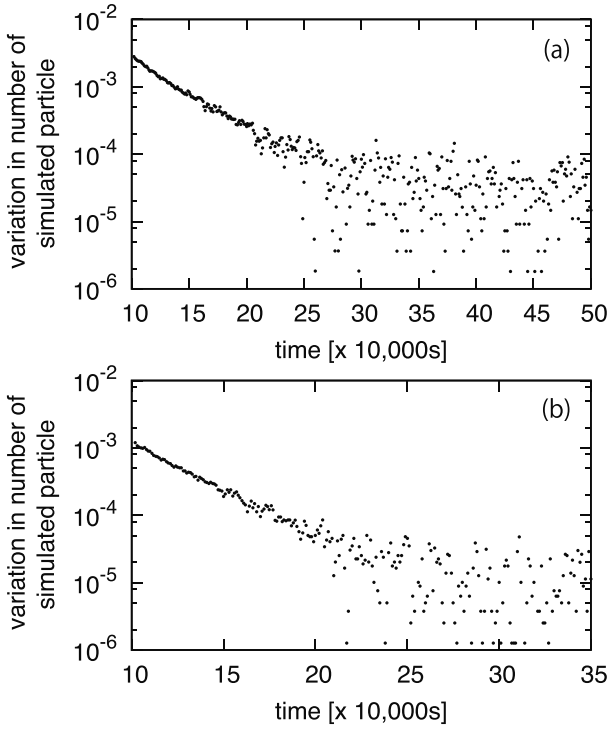

Figure 1. Time variations in the ratio of the number of model particles to that in the previous time step (a) for the 1 EUV case and (b) for the 6 EUV case.

reaches a quasi-steady state. Figure 1 shows the ratio of the number of model particles to that obtained in the previous time step. After $t = 250{,}000$ s for the 1 EUV case and $t = 220{,}000$ s for the 6 EUV case, variations in the total number of model particles are less than 0.01%, suggesting that the system reaches a quasi-steady state.

4. Ionosphere Model

To solve the hot O production due to the O_2^+ dissociative recombination in the DSMC simulation, a photochemical equilibrium ionosphere model runs simultaneously. Using the ionosphere model, the following values are computed: photoionization rates, chemical production and loss rates, and photochemical equilibrium densities of the major ionospheric constituents, H^+, O_2^+, O^+, CO_2^+, and electron.

Solar EUV flux is given for a 60° solar zenith angle. We calculate the EUV absorption using the solar EUV flux model and photoionization and photoabsorption cross sections from the EUVAC model [*Richards et al.*, 1994; *Schunk and Nagy*, 2000] and the neutral densities computed by the DSMC model. In the EUVAC model, solar activity variation is expressed by the following factor:

$$P = (F_{10.7} + \langle F_{10.7} \rangle)/2, \tag{13}$$

where $F_{10.7}$ is the 10.7 cm solar radio flux in W $Hz^{-1}m^{-2}$, multiplied by 10^{22}, and $<F10.7>$ is the $F_{10.7}$ flux averaged over 81 days. P is set at 69 for the 1 EUV case, and the solar EUV flux is scaled to the Mars' orbit by multiplying $(1/1.524)^2$ to that at the Earth's orbit. For the 6 EUV case, the solar EUV flux for the 1 EUV case is multiplied by 6.

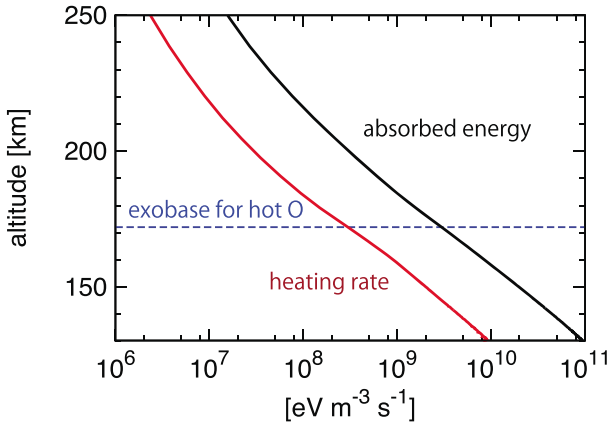

Figure 2. Altitude profiles of the heating rate owing to the dissociative recombination of O_2^+ calculated by the DSMC model (red curve), the total solar EUV energy absorbed by all species in the Martian upper thermosphere-exosphere per second (black curve), and the exobase for hot O atoms (blue dashed line) for the 1 EUV case.

The chemical reaction coefficients used in the ionosphere model are summarized in Table 1. The neutral temperature is computed in the DSMC model. The ion and electron temperatures are estimated following the method used in *Fox and Haćć* [2010] for obtaining the ion and electron temperatures at high solar activity. More specifically, ion and electron temperatures are increased from the low solar activity temperatures by the difference between the computed neutral temperature and the low solar

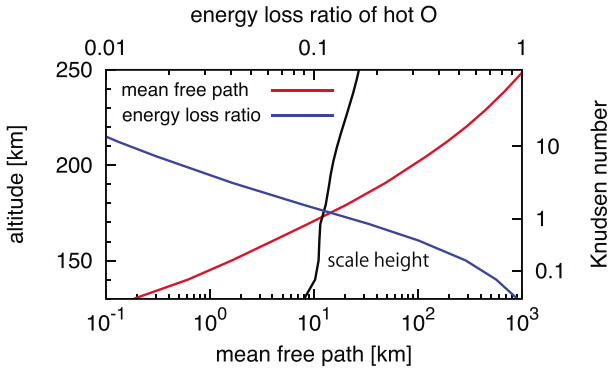

Figure 3. Altitude profiles of the mean free path of hot O with energy of 2 eV (red curve), the scale height (black curve), and the ratio between the total energy of hot O loss integrated over 1 s and the total energy of hot O existing at a given altitude (blue curve) computed by the DSMC model for the 1 EUV case. The Knudsen number is defined as the ratio of the mean free path to the scale height.

activity neutral temperature. The low solar activity neutral, ion, and electron temperatures are taken from *Shinagawa and Cravens* [1989], which are based on the Viking 1 and 2 measurements. Finally, assuming a photochemical equilibrium, the densities of H^+, O_2^+, O^+, CO_2^+, and electron are obtained.

5. Results and Discussion

5.1. Viking 1 Condition (1 EUV Case)

Figure 2 shows the altitude profiles of the heating rate owing to the O_2^+ dissociative recombination computed by the DSMC model and of the total solar EUV energy absorbed by all species in the Martian upper thermosphere-exosphere per second for the 1 EUV case. The heating rate is calculated by averaging the energy loss of hot O atoms in collisions with H, CO_2, N_2, and thermal O in the DSMC simulation. The total solar EUV energy absorbed is calculated in the ionosphere model. Below the exobase for hot O (172 km altitude, see discussion of Figure 3), the heating efficiency owing to the dissociative recombination of O_2^+ is about 0.1, where the heating efficiency is defined as the ratio of the heating rate divided by the total solar EUV energy absorbed by all species per second. Adding the other minor heating sources, the total heating efficiency is 0.18, which is in good agreement with the conventional value [*Fox and Dalgarno*, 1979; *Zhang et al.*, 1993]. Above the exobase, the atmospheric heating is less effective because there are fewer molecules to interact with for depositing the hot O energy.

Figure 3 shows the altitude profiles of the mean free path of hot O with energy of 2 eV and the scale height of the atmosphere. Here the mean free path and the scale height are defined as the mean distance traveled by a molecule between collisions and the distance over which the total neutral density decreases by a factor of *e*, respectively. The mean free path is computed by test particle simulations, which are separately carried out to track trajectories and collisions of 200,000 hot O particles in the background atmosphere obtained by a DSMC simulation (see Figure 4). The blue curve in Figure 3 shows the ratio of the energy loss of hot O integrated over 1 s divided by the total energy of hot O existing at a given altitude, where the energy loss of hot O is the same as the heating rate owing to hot O in Figure 2 when integrated over 1 s. At 130 km altitude, the Knudsen number of hot O is 0.025, indicating that collisions are dominant there. At that altitude, the energy loss rate of hot O is equal to 1, indicating that almost all the hot O produced by the O_2^+ dissociative recombination is thermalized immediately. The higher the altitude, the larger the Knudsen number, and the percentage of the energy lost to the total energy of hot O decreases. At 172 km altitude, where the Knudsen number is 1, i.e., the theoretical exobase for hot O, 15% of the total energy of hot O is deposited to the ambient atmosphere. At 210 km altitude, the Knudsen number is 10, and only 1% of the total energy of hot O changes to thermal energy. Above that altitude, the energy of hot O is hardly lost through collisions.

Figure 4 shows the altitude profiles of (a) densities, (b) vertical flow velocities, and (c) temperatures of H, CO_2, N_2, and O computed by the DSMC model. We illustrate only the results within the altitude range for which a cell contains a sufficient number of model particles (specifically, more than 30 particles in a cell for each molecular species). The measured densities of CO_2 and N_2 by Viking 1 [*Nier and McElroy*, 1977] are also shown in Figure 4a. The calculated densities of CO_2 and N_2 are in good agreement with the observed densities. The O and H densities are consistent with those in *Shinagawa and Cravens* [1989] and *Zhang et al.* [1993] that were estimated based on Viking and Mariner measurements, but the H density differs by a factor of 5.7 from that in *Fox and Hać* [2009]. The reason for the discrepancy in the H density between *Fox and Hać* [2009] and our model is mainly due to different lower boundary conditions for the H density used in the models.

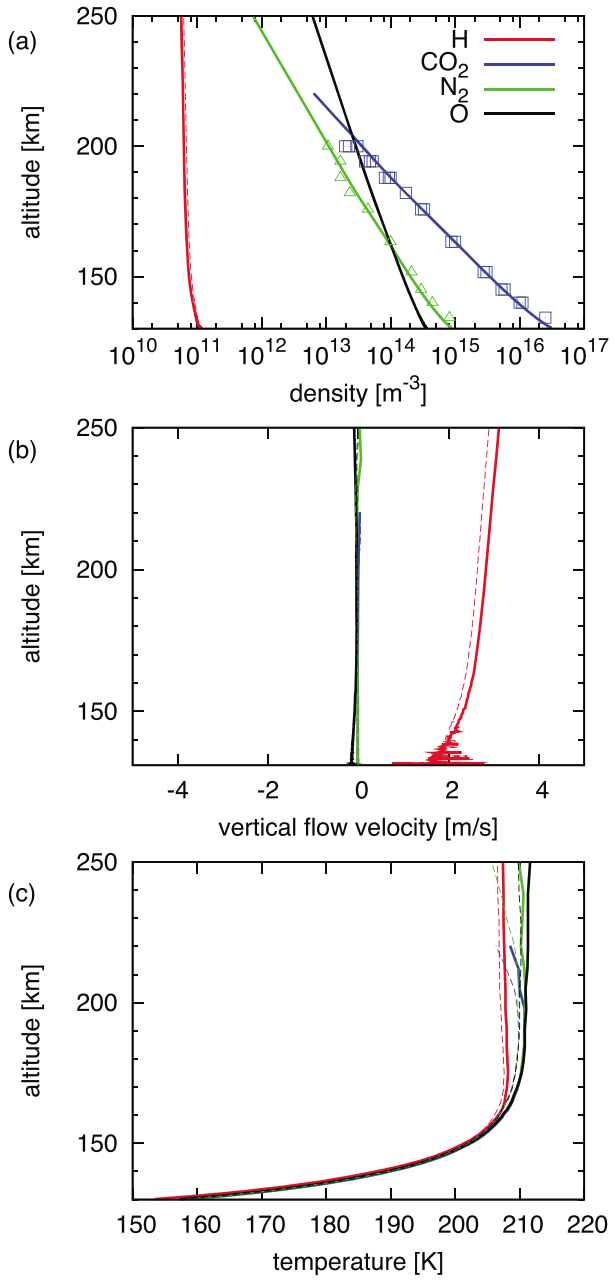

Figure 4. Altitude profiles of (a) densities, (b) vertical flow velocities, and (c) temperatures of H (red curve), CO_2 (blue curve), N_2 (green curve), and O (black curve) computed by the DSMC model for the 1 EUV case. The dashed curves show the results from the conventional model. The open squares and triangles in Figure 4a are the CO_2 and N_2 densities, respectively, measured by Viking 1 [*Nier and McElroy*, 1977].

The altitude profiles of O_2^+ and CO_2^+ computed by the ionosphere model as well as the measured densities of O_2^+ and CO_2^+ from Viking 1 and 2 [*Hanson et al.*, 1977] are shown in Figure 5. The calculated density of O_2^+, which is used to calculate the dissociative recombination of O_2^+, is in good agreement with the observed densities.

We note a difference in the vertical velocities between H and the others (Figure 4b). Only H has an upward flow; meanwhile, the others have negligible flows. The upward flow is caused by Jeans escape. In the present model, only H escapes to space by thermal energy and a hydrostatic equilibrium of H is not established [cf. *Tucker et al.*, 2013]. The exobase temperature of H in Figure 4c is about 2 K lower than that of the others. This difference is caused by the energy-dependent nature of Jeans escape and discussed in the next section.

Figure 6 shows the altitude profiles of the mean free path of each species and the scale height. The method for calculating the mean free paths is the same as that in Figure 3. In the test particle simulations for each mean free path, the distribution of the initial velocities of the test particles is taken from a Maxwell-Boltzmann distribution. The mean free paths for H, CO_2, N_2, and thermal O are different for different molecules because the collision cross sections are different. The exobase altitudes are defined as the altitudes where the mean free paths are equal to the density scale height. The exobase altitudes for H, CO_2, N_2, and thermal O are 182 km, 202 km, 194 km, and 190 km, respectively. The exobase temperatures are 210.5 K for CO_2, N_2, and O and 208 K for H. These are in good agreement with the exobase temperature of 200 K estimated from the Viking 1 observation [*Shinagawa and Cravens*, 1989; *Fox and Hać*, 2010].

We also perform a DSMC simulation that does not calculate the energy deposition from hot O but uses the conventional total heating efficiency of 0.18 (hereinafter referred to as the conventional model). The total heating efficiency of 0.18 is the same as that used in *Zhang et al.* [1993]. The results from the conventional model are

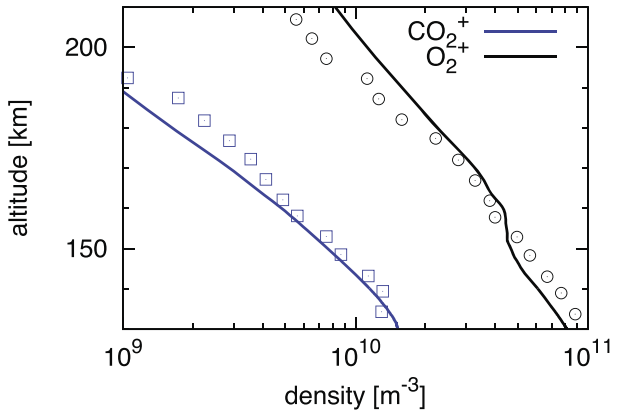

Figure 5. Altitude profiles of densities of CO_2^+ (blue curve) and O_2^+ (black curve) computed by the ionosphere model for the 1 EUV case. The open squares and circles are the CO_2^+ and O_2^+ densities, respectively, measured by Viking 1 and 2 [*Hanson et al.*, 1977].

also plotted with dashed curves in Figure 4. In Figures 4a and 4b, the blue, green, and black dashed curves almost overlap with the solid curves of the same color, and only the solid curves can be seen. The computed exobase temperature is 210 K, which matches well the temperature estimated by *Zhang et al.* [1993]. The altitude profiles of densities, flow velocities, and temperatures computed by the DSMC model that calculates the energy deposition from hot O are in good agreement with those computed by the conventional model, suggesting that the use of the conventional heating efficiency is a good approximation for the 1 EUV case.

5.2. Six Times the Solar EUV Flux of the Viking 1 Case (6 EUV Case)

Figure 7 shows the computed altitude profiles of (a) densities, (b) vertical flow velocities, and (c) temperatures for the 6 EUV case. The stronger EUV flux leads to an increase in the atmospheric temperature and expansion of the atmosphere. The H density decreases, however, due to increases in the Jeans escape rate and upward flow of H.

Above 200 km altitude, the temperature of H calculated using equation (3) decreases because of a decrease in the high-energy part of the velocity distribution due to Jeans escape. In these altitudes, the computed energy distribution of H is not consistent with a Maxwell-Boltzmann distribution. Figure 8a shows the computed thermal energy distribution of H at 300 km altitude. We see a clear depletion in the computed distribution above the escape velocity of about 5 km/s because of its preferential escape to space. Figure 8b shows that the low-energy part of the distribution, which is less affected by the Jeans escape, is in good agreement with the Maxwell-Boltzmann distribution with a temperature of 357 K, which is deduced from a fit at the most probable velocity.

The altitude variation of H temperatures deduced from a fit with a Maxwell-Boltzmann distribution at the most probable velocity is plotted in Figure 7c. These temperatures are higher than the temperatures computed using equation (3), but they remain lower than the temperatures of the other molecules. Above 200 km altitude, the Knudsen number of H becomes greater than 0.1 and H atoms have a global upward motion. H is not well heated by hot O and slightly cooled by heat advection.

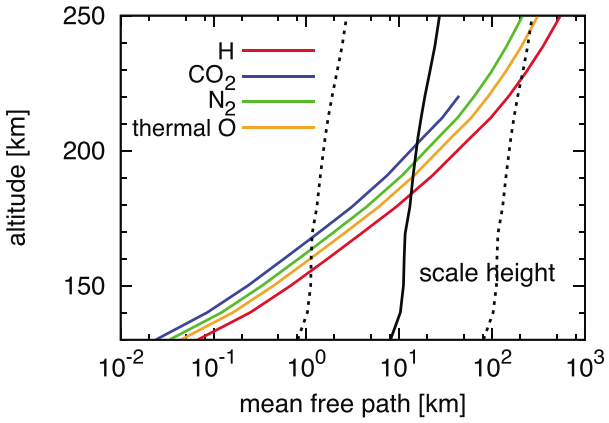

Figure 6. Computed altitude profiles of the mean free paths of H (red curve), CO_2 (blue curve), N_2 (green curve), and thermal O (yellow curve) and the scale height (black curve) for the 1 EUV case. The dotted curves represent 0.1 and 10 times the scale height, respectively.

For the 1 EUV case, there is less discrepancy between the computed distribution of H and a Maxwell-Boltzmann distribution. The exobase temperature of H deduced from a fit with a Maxwell-Boltzmann distribution at the most probable velocity is 210.5 K. It is about 2 K higher than the exobase temperature (Figure 4c) calculated using equation (3) and equal to the exobase temperature of the other species.

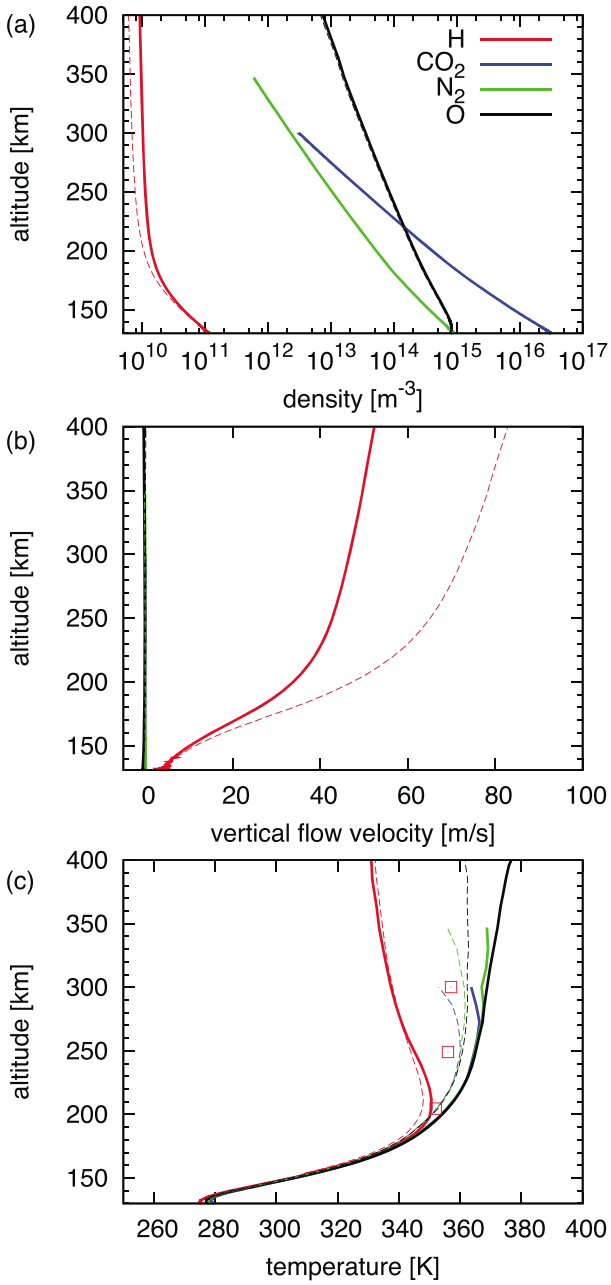

Figure 7. The same format as Figure 4 but for the 6 EUV case. The open squares in Figure 7c are the H temperatures deduced from a fit with a Maxwell-Boltzmann distribution at the most probable velocity.

Figure 9 shows the altitude profiles of the mean free path of each species and the scale height for the 6 EUV case. The exobase altitudes of H, CO_2, N_2, and thermal O are 246 km, 306 km, 300 km, and 272 km, respectively. The exobase temperatures of CO_2, N_2, and thermal O are about 360 K to 370 K. The temperature and the mean free path of CO_2 around the exobase altitude are not plotted because a statistical error is not negligible due to insufficient numbers of simulation particles for CO_2 contained in the cells. Nonetheless, the simulation model works properly because CO_2 is a minor component at that altitude.

Figure 10a shows the computed altitude profile of the mean free path of hot O with energy of 2 eV and the scale height for the 6 EUV case, and Figure 10b shows the heating efficiencies owing to the O_2^+ dissociative recombination for the 1 EUV case and the 6 EUV case. Below the exobase altitude, the heating efficiency

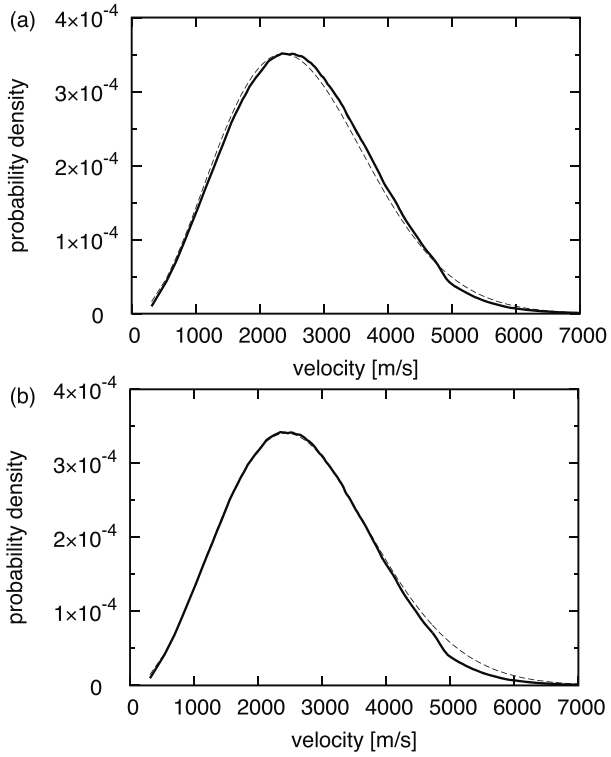

Figure 8. (a) Computed thermal energy distributions of H at 300 km altitude for the 6 EUV case. The dashed curve represents the Maxwell-Boltzmann distribution with a temperature of 337 K, which is obtained from equation (3). (b) Adjusted energy distribution of H at 300 km altitude, in which the height of the distribution is adjusted by taking into account the loss of escaping H atoms. The dashed curve represents the Maxwell-Boltzmann distribution with a temperature of 357 K, which is obtained from a fit at the most probable velocity.

owing to the dissociative recombination of O_2^+ for the 6 EUV case is about 1.1 times larger than that for the 1 EUV case, which results in the temperatures obtained by the DSMC model slightly deviating from those by the conventional model in and above the transition region (Figure 7c). Except for H atoms, the dashed curves in Figures 7a and 7b almost overlap with the solid curves and indicate that the conventional model is a good approximation also for the 6 EUV case.

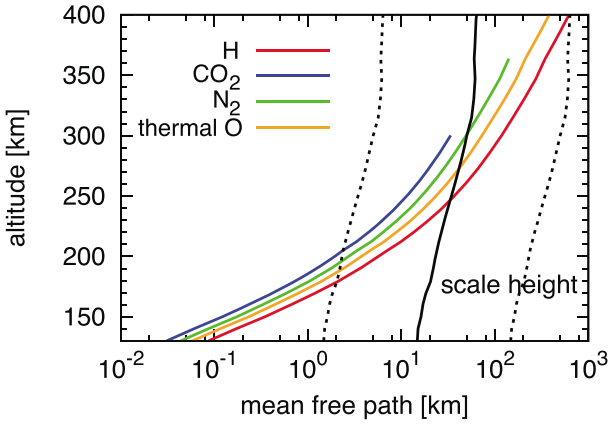

Figure 9. Computed altitude profiles of the mean free paths of H (red curve), CO_2 (blue curve), N_2 (green curve), and thermal O (yellow curve) and the scale height (black curve) for the 6 EUV case. The dotted curves represent 0.1 and 10 times the scale height, respectively.

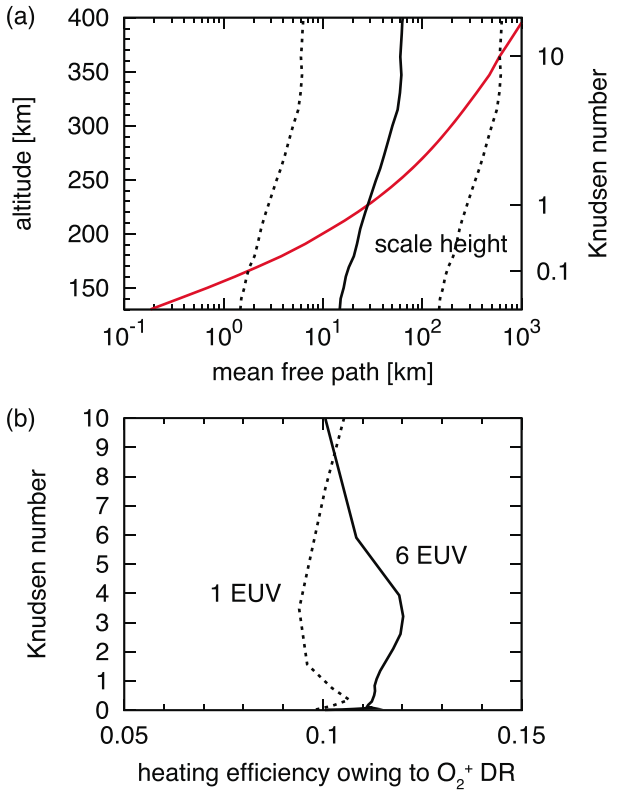

Figure 10. (a) Computed altitude profiles of the mean free path of hot O with energy of 2 eV (red curve) and the scale height (black curve) for the 6 EUV case. The dotted curves represent 0.1 and 10 times the scale height, respectively. (b) The heating efficiencies owing to the dissociative recombination of O_2^+ at the altitude corresponding to a given Knudsen number for the 6 EUV case (solid curve) and the 1 EUV case (dashed curve).

The more efficient heating at the 6 EUV case is due to two factors: enhanced photochemical reactions and a thicker transition region. The photochemical reactions transform the absorbed solar EUV energy into the energy of hot O produced by the dissociative recombination of O_2^+ more efficiently, because there are more O in the atmosphere for the 6 EUV case than for the1 EUV case. An increase in O density leads to an increase in O_2^+ density and hot O production rate due to the dissociative recombination of O_2^+, because O_2^+ is produced through the chemical reaction between CO_2^+ and O. Around the exobase level, the heating efficiency is apparently large, because hot O atoms that were originally produced in lower altitude deposit their energy into the ambient atmosphere. Note that in this study, only the dissociative recombination of O_2^+ is included as a kinetic heating source, and other photochemical reactions such as dissociative recombination of CO_2^+ [*Gröller et al.*, 2014] should be included in future studies.

Figure 11 shows the computed energy distribution of hot O existing at the exobase and hot O produced by the dissociative recombination of O_2^+ over 1 s at the exobase for the1 EUV and the 6 EUV cases. More hot O atoms that were originally produced in lower altitude populate at the exobase for the 6 EUV case than for the 1 EUV case, because the width of the transition region for the 6 EUV case is thicker than that for the 1 EUV case (Figures 3 and 10a). An increase in the atmospheric temperature leads to a thicker transition region.

Under an extremely strong solar EUV flux environment, we would expect a much more efficient photochemical hot O production and a much thicker transition region. The heating efficiency owing to the dissociative recombination during such an extremely strong EUV environment would be much larger than those for the 1 EUV and the 6 EUV cases. A simulation study of early Mars about 4.5 Gyr ago [e.g., *Terada et al.*, 2009], where up to ~100 times stronger solar EUV flux than today is expected, would require careful consideration of the appropriateness of applying the conventional model.

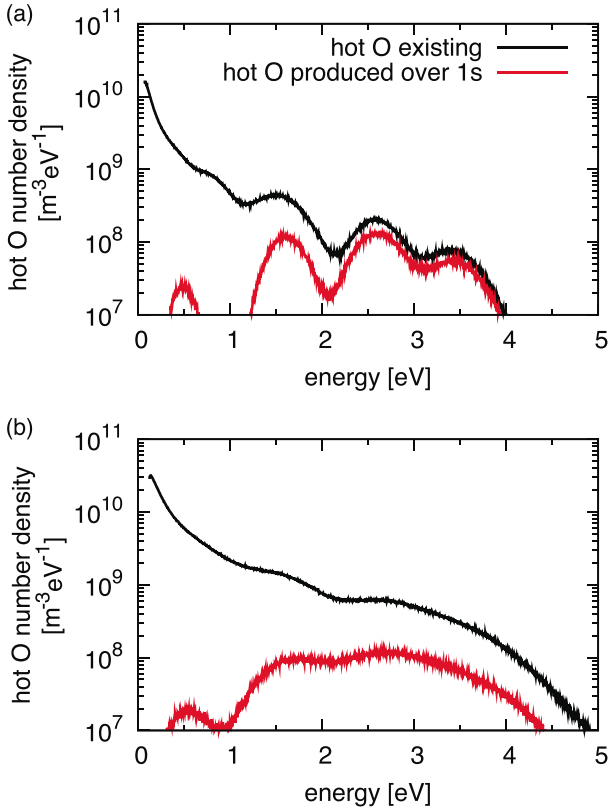

Figure 11. Calculated energy distribution of hot O existing at the exobase (black curve) and hot O produced by the dissociative recombination of O_2^+ over 1 s at the exobase (red curve) (a) for the 1 EUV case and (b) for the 6 EUV case.

The computed exobase temperatures of about 360 to 370 K for the 6 EUV case are much lower than the exobase temperature of 550 K estimated by *Zhang et al.* [1993], because the CO_2-O collisional energy transfer rate used in our model is different from that used in *Zhang et al.* [1993]. The CO_2-O collisional energy transfer rate of *Gordiets et al.* [1982] used in our model is a function of temperature and increases as temperature increases, while the rate in *Zhang et al.* [1993] seems independent of temperature. The energy transfer rate of *Gordiets et al.* [1982] for 200 K, which is the temperature of the upper thermosphere for the Viking 1 condition, is 2.7×10^{-13} cm^3 s^{-1}, and that for 550 K, which is the temperature of the upper thermosphere for the

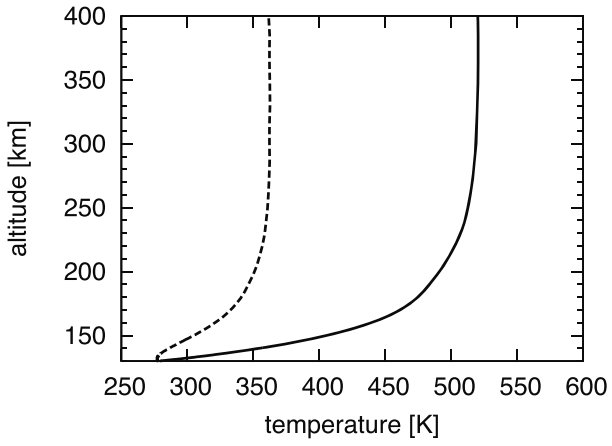

Figure 12. Altitude profiles of the O temperature calculated by the DSMC model for the 6 EUV case with the CO_2-O collisional energy transfer rate in *Dickinson and Bougher* [1986] (solid curve) and with that in *Gordiets et al.* [1982] (dashed curve).

6 EUV case estimated by *Zhang et al*. [1993], is 3.5×10^{-12} $cm^3 s^{-1}$. As discussed in *Bougher et al*. [2015], the importance of the CO_2 15 μm cooling is still uncertain. There is a large difference between different models of the CO_2-O collisional energy transfer rate. For example, the energy transfer rate of *Dickinson and Bougher* [1986] is 4.0×10^{-13} $cm^3 s^{-1}$, and that often used in current Martian GCM models is 3.0×10^{-12} $cm^3 s^{-1}$ [*Gonzalez-Galindo et al*., 2009; *Bougher et al*., 2015]. Figure 12 shows the calculated altitude profiles of O temperature. The solid curve represents the result using the rate of *Dickinson and Bougher* [1986], and the dashed curve represents the result using the rate of *Gordiets et al*. [1982]. The exobase temperature calculated using the rate of *Dickinson and Bougher* [1986] is 520 K. It is about 150 K higher than that using the rate of *Gordiets et al*. [1982] and in reasonable agreement with that of *Zhang et al*. [1993]. Under strong EUV flux environments, the CO_2 15 μm cooling is expected to have a large effect on the temperature of the upper thermosphere and exosphere.

6. Summary

We developed a full-particle model of the Martian upper thermosphere and exosphere. Unlike previous Martian thermosphere-exosphere models, no fluid approximation is invoked in our model, and the DSMC method is applied to both thermal and nonthermal components. The model can self-consistently solve the transition from collisional to collisionless domains in the upper thermosphere, so that the energy deposition from nonthermal hot components to thermal components in the transition region is properly described. Our model self-consistently solves heating by the dissociative recombination of O_2^+ and cooling by molecular conduction, which are the primary sources of the atmospheric heating and cooling in the Martian upper thermosphere, respectively, while other minor heating and cooling sources are included using macroscopic quantities.

For the solar EUV condition during the Viking 1 measurement (1 EUV case), the computed altitude profiles of CO_2 and N_2 densities are in good agreement with those observed by Viking 1. We also performed a DSMC simulation that does not calculate the energy deposition from hot O but uses a conventional heating efficiency of 0.18 as that used in *Zhang et al*. [1993]. The altitude profiles of densities, flow velocities, and temperatures computed by the DSMC model that calculates the energy deposition from hot O match well those computed by the conventional model, suggesting that the use of the conventional heating efficiency is a good approximation for the 1 EUV case.

For a solar EUV flux equivalent to 6 times the Viking 1 condition (6 EUV case), the heating efficiency computed by the DSMC model that calculates the energy deposition from hot O is essentially the same as that for the 1 EUV case, but slightly increases to about 110% of that for the 1 EUV case below the exobase, and the calculated temperature deviates from the conventional model in and above the transition region. The stronger EUV flux leads to a more efficient hot O production and a thicker transition region. These results suggest that the conventional heating efficiency of 0.18 obtained based on the observation of present-day Mars is a good approximation for low (1 EUV case) to moderately strong (6 EUV case) EUV conditions, but it would be inappropriate to apply to an early, extremely strong EUV flux environment.

At the exobase, the computed velocity distribution of H is not consistent with a Maxwell-Boltzmann distribution due to the preferential escape of the high-energy part of the distribution in the Jeans escape process. The difference between the computed distribution and the Maxwell-Boltzmann distribution is negligible for the 1 EUV case, but is noticeable for the 6 EUV case.

We also find that the exobase temperature calculated using the CO_2-O collisional energy transfer rate of *Gordiets et al*. [1982] is 150 K lower than that calculated using the rate of *Dickinson and Bougher* [1986] for the 6 EUV case. The latter is in reasonable agreement with the exobase temperature estimated by *Zhang et al*. [1993]. Under strong EUV flux environments, the CO_2 15 μm cooling is expected to have a large effect on the temperature of the upper thermosphere and exosphere.

Acknowledgments
This work was supported by Grant-in-Aid for JSPS Fellows 23. 3327 and for Scientific Research (B) 15H03731 from JSPS. This work is conducted partially under NASA's MAVEN Participating Scientist Program (Proposal 12-MAVENPS12-0017, K. Seki). The molecular dynamics simulation was carried out using the computer facilities at the Information Technology Center, Nagoya University. The DSMC simulation was carried out using the computer facilities at the Research Institute for Information Technology, Kyushu University. Both the input data and the methods used in this paper are properly cited and referred to in the reference list. The computed data are available from the authors upon request (kaneda@pat.gp.tohoku.ac.jp).

References

Bird, G. (1994), *Molecular Gas Dynamics and the Direct Simulation of Gas Flows*, Clarendon Press, Oxford.

Bougher, S. W., and R. E. Dickinson (1988), Mars mesosphere and thermosphere: 1. Global mean heat budget and thermal structure, *J. Geophys. Res.*, *93*, 7325–7337, doi:10.1029/JA093iA07p07325.

Bougher, S. W., and R. G. Roble (1991), Comparative terrestrial planet thermospheres: 1. Solar cycle variation of global mean temperatures, *J. Geophys. Res.*, *96*, 11,045–11,055, doi:10.1029/91JA01162.

Bougher, S. W., D. Pawlowski, J. M. Bell, S. Nelli, T. McDunn, J. R. Murphy, M. Chizek, and A. Ridley (2015), Mars Global Ionosphere-Thermosphere Model (MGITM): Solar cycle, seasonal, and diurnal variations of the Mars upper atmosphere, *J. Geophys. Res. Planets*, *120*, 311–342, doi:10.1002/2014JE004715.

Boushehri, A. J. B., J. Kestin, and E. A. Mason (1987), Equilibrium and transport properties of eleven polyatomic gases at low density, *J. Phys. Chem. Ref. Data*, *16*, 445–466.

Capitelli, M., C. Gorse, S. Longo, and D. Giordano (2000), Collision integrals of high-temperature air species, *J. Thermophys. Heat Transfer*, *14*, 259–268.

Chapman, S., and T. G. Cowling (1970), *The Mathematical Theory of Non-uniform Gases*, Cambridge Univ. Press, Cambridge.

Chaufray, J.-Y., R. Modolo, F. Leblanc, G. Chanteur, R. E. Johnson, and J. G. Luhmann (2007), Mars solar wind interaction: Formation of the Martian corona and atmospheric loss to space, *J. Geophys. Res.*, *112*, E09009, doi:10.1029/2007JE002915.

Chaufray, J.-Y., F. Gonzalez-Galindo, F. Forget, M. A. Lopez-Valverde, F. Leblanc, R. Modolo, and S. Hess (2015), Variability of the hydrogen in the Martian upper atmosphere as simulated by a 3D atmosphere-exosphere coupling, *Icarus*, *245*, 282–294, doi:10.1016/j.icarus.2014.08.038.

Cipriani, F., F. Lebranc, and J. J. Berthelier (2007), Martian corona: Nonthermal sources of hot heavy species, *J. Geophys. Res.*, *112*, E07001, doi:10.1029/2006JE002818.

Dickinson, R. E., and S. W. Bougher (1986), Venus mesosphere and thermosphere 1. Heat budget and thermal structure, *J. Geophys. Res.*, *91*, 70–80, doi:10.1029/JA091iA01p00070.

Fox, J. L. (1993), On the escape of oxygen and hydrogen from Mars, *Geophys. Res. Lett.*, *20*, 1847–1850, doi:10.1029/93GL01874.

Fox, J. L., and A. Dalgarno (1979), Ionization, luminosity, and heating of the upper atmosphere of Mars, *J. Geophys. Res.*, *84*, 7315–7333, doi:10.1029/JA084iA12p07315.

Fox, J. L., and A. B. Hać (2014), The escape of O from Mars: Sensitivity to the elastic cross sections, *Icarus*, *228*, 375–385, doi:10.1016/j.icarus.2013.10.014.

Fox, J. L., and A. Hać (2009), Photochemical escape of oxygen from Mars: A comparison of the exobase approximation to a Monte Carlo method, *Icarus*, *204*, 527–544, doi:10.1016/j.icarus.2009.07.005.

Fox, J. L., and A. Hać (2010), Isotope fractionation in the photochemical escape of O from Mars, *Icarus*, *208*, 176–191, doi:10.1016/j.icarus.2010.01.019.

Fox, J. L., and K. Y. Sung (2001), Solar activity variations of the Venus thermosphere/ionosphere, *J. Geophys. Res.*, *106*, 21,305–21,335, doi:10.1029/2001JA000069.

Gonzalez-Galindo, F., F. Forget, M. A. López-Valverde, M. Angelats i Coll, and E. Millour (2009), A ground-to-exosphere Martian circulation model: 1. Seasonal, diurnal and solar cycle variation of thermospheric temperatures, *J. Geophys. Res.*, *114*, E04001, doi:10.1029/2008JE003246.

Gordiets, B. F., Y. N. Kujikov, M. N. Markov, and M. Y. Marov (1982), Numerical modeling of the thermospheric heat budget, *J. Geophys. Res.*, *87*, 4504–4514, doi:10.1029/JA087iA06p04504.

Gröller, H., H. Lichtenegger, H. Lammer, and V. I. Shematovich (2014), Hot oxygen and carbon escape from the Martian atmosphere, *Planet. Space Sci.*, *98*, 93–105.

Hanson, W. B., S. Sanatani, and D. R. Zuccaro (1977), The Martian ionosphere as observed by the Viking retarding potential analyzers, *J. Geophys. Res.*, *82*, 4351–4363, doi:10.1029/JS082i028p04351.

Hirschfelder, J. O., C. F. Curtiss, and R. B. Bird (1964), *Molecular Theory of Gases and Liquids*, John Wiley, New York.

Hodges, R. R. (2000), Distributions of hot oxygen for Venus and Mars, *J. Geophys. Res.*, *105*, 6971–6981, doi:10.1029/1999JE001138.

Ip, W.-H. (1988), On a hot oxygen corona of Mars, *Icarus*, *76*, 134–145.

Kaneda, K., N. Terada, and S. Machida (2007), Time variation of nonthermal escape of oxygen from Mars after solar wind dynamic pressure enhancement, *Geophys. Res. Lett.*, *34*, L20201, doi:10.1029/2007GL030576.

Kaneda, K., N. Terada, and S. Machida (2009), Solar-wind control of the hot oxygen corona around Mars, *J. Geophys. Res.*, *114*, E02007, doi:10.1029/2008JE003234.

Kella, D., L. Vejby-Christensen, P. J. Johnson, H. B. Pedersen, and L. H. Andersen (1997), The source of green light emission determined from a heavy-ion storage ring experiment, *Science*, *276*, 1530–1533.

Kim, J., A. F. Nagy, J. L. Fox, and T. E. Cravens (1998), Solar cycle variability of hot oxygen atoms at Mars, *J. Geophys. Res.*, *103*, 29,339–29,342, doi:10.1029/98JA02727.

Lammer, H., and S. J. Bauer (1991), Nonthermal atmospheric escape from Mars and Titan, *J. Geophys. Res.*, *96*, 1819–1825, doi:10.1029/90JA01676.

Lammer, H., W. Stumptner, and S. J. Bauer (2000), Upper limits for the Martian exospheric number density during the planet B/Nozomi mission, *Planet. Space Sci.*, *48*, 1473–1478.

Lammer, H., H. I. M. Lichtenegger, C. Kolb, I. Ribas, E. F. Guinan, R. Abart, and S. J. Bauer (2003), Loss of water from Mars: Implications for the oxidation of the soil, *Icarus*, *165*, 9–25.

Leblanc, F., and R. E. Johnson (2001), Sputtering of the Martian atmosphere by solar wind pick-up ions, *Planet. Space Sci.*, *49*, 645–656.

Leblanc, F., and R. E. Johnson (2002), Role of molecular species in pickup ion sputtering of the Martian atmosphere, *J. Geophys. Res.*, *107*(E2), 5010, doi:10.1029/2000JE001473.

Lee, Y., M. R. Combi, V. Tenishev, and S. W. Bougher (2014a), Hot carbon corona in Mars' upper thermosphere and exosphere: 1. Mechanisms and structure of the hot corona for low solar activity at equinox, *J. Geophys. Res. Planets*, *119*, 905–924, doi:10.1002/2013JE004552.

Lee, Y., M. R. Combi, V. Tenishev, and S. W. Bougher (2014b), Hot carbon corona in Mars' upper thermosphere and exosphere: 2. Solar cycle and seasonal variability, *J. Geophys. Res. Planets*, *119*, 2487–2509, doi:10.1002/2014JE004669.

Lee, Y., M. R. Combi, V. Tenishev, S. W. Bougher, and R. J. Lillis (2015), Hot oxygen corona at Mars and the photochemical escape of oxygen: Improved description of the thermosphere, ionosphere, and exosphere, *J. Geophys. Res. Planets*, *120*, 1880–1892, doi:10.1002/2015JE004890.

Luhmann, J. G. (1997), Correction to "The ancient oxygen exosphere of Mars: Implications for atmosphere evolution" by Zhang et al, *J. Geophys. Res.*, *102*, 1637, doi:10.1029/96JE03440.

Luhmann, J. G., and J. U. Kozyra (1991), Dayside pickup oxygen precipitation at Venus and Mars: Spatial distributions, energy deposition and consequences, *J. Geophys. Res.*, *96*, 5457–5467, doi:10.1029/90JA01753.

Luhmann, J. G., R. E. Johnson, and M. H. G. Zhang (1992), Evolutionary impact of sputtering of the Martian atmosphere by O^+ pickup ions, *Geophys. Res. Lett.*, *19*, 2151–2154, doi:10.1029/92GL02485.

Lundin, R., A. Zakharov, R. Pellinen, H. Borg, B. Hultqvist, N. Pissarenko, E. M. Dubinin, S. Barabash, I. Liede, and H. Koskinen (1989), First measurement of the ionospheric plasma escape from Mars, *Nature*, *341*, 609–612.

Lundin, R., S. Barabash, M. Holmstrom, H. Nilsson, M. Yamauchi, M. Fraenz, and E. M. Dubinin (2008), A comet-like escape of ionospheric plasma from Mars, *Geophys. Res. Lett.*, *35*, L18203, doi:10.1029/2008GL034811.

Mahaffy, P. R., M. Benna, M. Elrod, R. V. Yelle, S. W. Bougher, S. W. Stone, and B. M. Jakosky (2015), Structure and composition of the neutral upper atmosphere of Mars from the MAVEN NGIMS investigation, *Geophys. Res. Lett.*, *42*, 8951–8957, doi:10.1002/2015GL065329.

Matsumoto, H. (2002), Variable sphere molecular model for inverse power law and Lennard-Jones potentials in Monte Carlo simulations, *Phys. Fluids*, *14*, 4256–4265.

McElroy, M. B. (1972), Mars: An evolving atmosphere, *Science*, *175*, 443–445.

Modolo, R., G. M. Chanteur, E. Dubinin, and A. P. Matthews (2005), Influence of the solar EUV flux on the Martian plasma environment, *Ann. Geophys.*, *23*, 433–444.

Nagy, A. F., and T. E. Cravens (1988), Hot oxygen atoms in the upper atmospheres of Venus and Mars, *Geophys. Res. Lett.*, *15*, 433–435, doi:10.1029/GL015i005p00433.

Nanbu, K., and S. Yonemura (1998), Weighted particles in Coulomb collision simulations based on the theory of a cumulative scattering angle, *J. Comput. Phys.*, *145*, 639–654.

Nier, A. O., and M. B. McElroy (1977), Composition and structure of Mars' upper atmosphere: Results from the neutral mass spectrometers on Viking 1 and 2, *J. Geophys. Res.*, *82*, 4341–4349, doi:10.1029/JS082i028p04341.

Perez-de-Tejada, H. (1987), Plasma flow in the Mars magnetosphere, *J. Geophys. Res.*, *92*, 4713–4718, doi:10.1029/JA092iA05p04713.

Perez-de-Tejada, H. (1992), Solar wind erosion of the Mars early atmosphere, *J. Geophys. Res.*, *97*, 3159–3167, doi:10.1029/91JA01985.

Peverall, R., et al. (2000), Dissociative recombination and excitation of O_2^+: Cross sections, product yields and implications for studies of ionospheric airglows, *J. Chem. Phys.*, *114*, 6679–6689.

Ribas, I., E. F. Guinan, M. Gudel, and M. Audard (2005), Evolution of the solar activity over time and effects on planetary atmospheres: I. High-energy irradiances (1–1700 A), *Astrophys. J.*, *622*, 680–694, doi:10.1086/427977.

Richards, P. G., J. A. Fennelly, and D. G. Torr (1994), EUVAC: A solar EUV flux model for aeronomic calculations, *J. Geophys. Res.*, *99*, 8981–8992, doi:10.1029/94JA00518.

Schunk, R. W., and A. F. Nagy (1980), Ionospheres of the terrestrial planets, *Rev. Geophys.*, *18*, 813–852, doi:10.1029/RG018i004p00813.

Schunk, R. W., and A. F. Nagy (2000), *Ionospheres: Physics, Plasma Physics and Chemistry*, Cambridge Univ. Press, Cambridge, U. K.

Shinagawa, H., and T. E. Cravens (1989), A one-dimensional multispecies magnetohydrodynamic model of the dayside ionosphere of Mars, *J. Geophys. Res.*, *94*, 6506–6516, doi:10.1029/JA094iA06p06506.

Shizgal, B. D., and G. G. Arkos (1996), Nonthermal escape of the atmospheres of Venus, Earth, and Mars, *Rev. Geophys.*, *34*, 483–505, doi:10.1029/96RG02213.

Svehla, R. A. (1962), Estimated viscosities and thermal conductivities of gases at high temperatures NASA Tech. Rep., R-132.

Terada, N., Y. N. Kulikov, H. Lammer, H. I. M. Lichtenegger, T. Tanaka, H. Shinagawa, and T. Zhang (2009), Atmosphere and water loss from early Mars under extreme solar wind and EUV conditions, *Astrobiology*, *9*, 55–70, doi:10.1089/ast.2008.0250.

Tucker, O. J., R. E. Johnson, J. I. Deighan, and A. N. Volkov (2013), Diffusion and thermal escape of H_2 from Titan's atmosphere: Monte Carlo simulations, *Icarus*, *222*, 149–158, doi:10.1016/j.icarus.2012.10.016.

Valeille, A., V. Tenishev, S. W. Bougher, M. R. Combi, and A. F. Nagy (2009a), Three-dimensional study of Mars upper thermosphere/ionosphere and hot oxygen corona: 1. General description and results at equinox for solar low conditions, *J. Geophys. Res.*, *114*, E11005, doi:10.1029/2009JE003388.

Valeille, A., M. R. Combi, S. W. Bougher, V. Tenishev, and A. F. Nagy (2009b), Three-dimensional study of Mars upper thermosphere/ionosphere and hot oxygen corona: 2. Solar cycle, seasonal variations, and evolution over history, *J. Geophys. Res.*, *114*, E11006, doi:10.1029/2009JE003389.

Valeille, A., M. R. Combi, V. Tenishev, S. W. Bougher, and A. F. Nagy (2010a), A study of suprathermal oxygen atoms in Mars upper thermosphere and exosphere over the range of limiting conditions, *Icarus*, *206*, 18–27, doi:10.1016/j.icarus.2008.08.018.

Valeille, A., M. R. Combi, V. Tenishev, S. W. Bougher, and A. F. Nagy (2010b), Water loss and evolution of the upper atmosphere and exosphere over Martian history, *Icarus*, *206*, 28–39, doi:10.1016/j.icarus.2009.04.036.

Yagi, M., F. Leblanc, J. Y. Chaufray, F. Gonzalez-Galindo, S. Hess, and R. Modolo (2012), Mars exospheric thermal and non-thermal components: Seasonal and local variations, *Icarus*, *221*, 682–693, doi:10.1016/j.icarus.2012.07.022.

Zahnle, K. J., and J. C. G. Walker (1982), The evolution of solar ultraviolet luminosity, *Rev. Geophys.*, *20*, 280–292, doi:10.1029/RG020i002p00280.

Zhang, M. H. G., J. G. Luhmann, S. W. Bougher, and A. F. Nagy (1993), The ancient oxygen exosphere of Mars: Implications for atmosphere evolution, *J. Geophys. Res.*, *98*, 10,915–10,923, doi:10.1029/93JE00231.